Phase-field simulations of dendritic crystal growth in a forced flow

X. Tong,[1] C. Beckermann,[1,*] A. Karma,[2] and Q. Li[1]
[1]*Department of Mechanical Engineering, University of Iowa, Iowa City, Iowa 52242*
[2]*Department of Physics and Center for Interdisciplinary Research on Complex Systems, Northeastern University, Boston, Massachusetts 02115*

(Received 7 August 2000; revised manuscript received 31 January 2001; published 15 May 2001)

Convective effects on free dendritic crystal growth into a supercooled melt in two dimensions are investigated using the phase-field method. The phase-field model incorporates both melt convection and thermal noise. A multigrid method is used to solve the conservation equations for flow. To fully resolve the diffuse interface region and the interactions of dendritic growth with flow, both the phase-field and flow equations are solved on a highly refined grid where up to 2.1 million control volumes are employed. A multiple time-step algorithm is developed that uses a large time step for the flow-field calculations while reserving a fine time step for the phase-field evolution. The operating state (velocity and shape) of a dendrite tip in a uniform axial flow is found to be in quantitative agreement with the prediction of the Oseen-Ivantsov transport theory if a tip radius based on a parabolic fit is used. Furthermore, using this parabolic tip radius, the ratio of the selection parameters without and with flow is shown to be close to unity, which is in agreement with linearized solvability theory for the ranges of the parameters considered. Dendritic sidebranching in a forced flow is also quantitatively studied. Compared to a dendrite growing at the same supercooling in a diffusive environment, convection is found to increase the amplitude and frequency of the sidebranches. The phase-field results for the scaled sidebranch amplitude and wavelength variations with distance from the tip are compared to linear Wentzel-Kramers-Brillouin theory. It is also shown that the asymmetric sidebranch growth on the upstream and downstream sides of a dendrite arm growing at an angle with respect to the flow can be explained by the differences in the mean shapes of the two sides of the arm.

DOI: 10.1103/PhysRevE.63.061601 PACS number(s): 68.70.+w, 81.30.Fb

I. INTRODUCTION

Free dendritic growth of a crystal into a supercooled melt involves two inherently coupled processes: the steady-state growth of the dendrite tip and the time-dependent sidebranching development. The dendrite tip is usually characterized by its operating state: growth velocity and tip shape. In the absence of flow, microscopic solvability theory [1–3] has successfully clarified the crucial role played by crystalline anisotropy in the tip selection, and this theory has been confirmed by phase-field simulations in two [4,5] and three [6] dimensions. Dendritic sidebranches are primarily important to metallurgists because they determine the microstructure and microsegregation patterns in metals and alloys.

Convective flow usually accompanies dendritic crystal growth. In fact, all dendritic growth data acquired under terrestrial conditions are found to deviate from the predictions of diffusion theories at low supercoolings [7–10]. Convection in the melt is believed to be responsible for that deviation. The effects of convection on dendritic growth and pattern formation have been an active research topic for many years, but have not been fully understood. Experimental investigations of the operating state of a dendrite tip in the presence of a forced flow have failed to yield consistent results. Bouissou *et al.* [11] found that the inverse of the selection parameter $1/\sigma^* \sim \rho^2 V$, where ρ and V denote the tip radius and velocity, respectively, increases for pivalic acid (PVA) dendrites almost linearly with the longitudinal component of the external flow velocity, but is independent of the transverse component of the flow velocity. Emsellem and Tabeling [12] performed growth experiments using ammonium bromide and found $1/\sigma^*$ to be almost independent of the external flow velocity in their experimental range. On the other hand, the experiments on succinonitrile (SCN) by Lee *et al.* [13] and Ananth and Gill [14] indicate that $1/\sigma^*$ decreases, rather than increases, with increasing flow velocity.

On the theoretical side, the presence of melt convection considerably complicates the tip-selection problem. Theoretical models have been developed to predict how heat transport away from the tip is modified by flow in various situations [15–21]. Ben Amar and Pomeau [22] have proposed scaling laws to characterize the tip-operating state in different regimes. Bouissou and Pelce [23] have extended the linearized solvability theory, which assumes a parabolic tip shape, to make quantitative predictions of tip selection for the case of a uniform axial flow in two dimensions. A rigorous treatment of dendritic growth with flow, however, has remained lacking. Melt convection adds new length and time scales to the problem and could lead to the formation of completely different dendritic patterns in comparison to the purely diffusive case.

The formation and development of sidebranches are generally attributed to the Mullins-Sekerka instability [24]. Sidebranching is believed to initiate from thermal noise intrinsically present in a solidification system. Langer and coworkers [25–27] theoretically investigated the selective amplification of thermal noise near the tip of an axisymmetric dendrite. Brener and Temkin [28] showed that quantita-

*Corresponding author. FAX: (319) 335-5669. Email address: becker@engineering.uiowa.edu

tive agreement with experiments could only be achieved by taking into account the nonaxisymmetric shape of dendrites. Many experiments have been performed to study dendritic sidebranching behavior for a variety of materials [7,29–31]. Dougherty *et al.* [29] studied the growth of ammonium bromide dendrites and found that sidebranches are not periodic at any distance from the tip, with apparently random variations in both phase and amplitude. Bouissou *et al.* [30] investigated dendrites of pivalic acid under the influence of a periodic forcing flow and found that the dendrites behave just like a linear selection amplifier, which is in qualitative agreement with linear WKB theory. Bisang and Bilgram [31] measured the tip shape and sidebranches of xenon dendrites, and obtained quantitative agreement with the theory of Brener and Temkin [28] for thermal noise amplification along a nonaxisymmetric dendrite.

The phase-field method has emerged as a powerful tool for numerically simulating dendritic growth [32–38]. Through the introduction of a phase-field variable to distinguish between the solid and liquid phases, the method provides a continuum description of phase transformation, and the complicated topological changes of a solid-liquid interface can be handled easily without the need to track the interface. Recently, phase-field models for solidification have been extended to include melt convection [39–41], providing a novel approach to study the interactions of dendritic growth and melt convection.

The objective of this paper is to present a quantitative study of free dendritic growth of a pure substance in a forced flow in two dimensions using the phase-field method. Both the tip-operating state and the sidebranching development in a forced flow are investigated. While we presented some of our results on the tip-operating state in the presence of flow in a recent communication [42], this full-length paper provides a more detailed account of the work and also includes sidebranching. To our knowledge, the only previous study using the phase-field method for simulating dendritic growth with melt convection is by Tonhardt and Amberg [40], who focused on dendritic growth from a wall inside a channel. They found that sidebranching is promoted on the upstream side and inhibited on the downstream side, but no quantitative comparison was made with existing sharp interface theories.

The present paper is organized as follows. Following this Introduction, Sec. II gives the formulation of the phase-field model that incorporates both melt convection and thermal noise quantitatively. The asymptotics of the phase-field model are also reviewed. Section III discusses the numerical issues related to the present phase-field and flow-field calculations along with the problem description. Section IV focuses on the tip-operating state in a forced flow, and comparisons of the numerical predictions with the analytical two-dimensional Oseen-Ivantsov and linearized solvability theories for tip growth in an axial flow are made. The sidebranching development due to the introduction of thermal noise is discussed in Sec. V, in which both the wavelength and amplitude of the sidebranches are studied as a function of the convection intensity and the thermal noise strength. A comparison with the linear WKB theory prediction is also made. Finally, some conclusions are drawn from the present investigation.

II. PHASE-FIELD MODEL

A. Incorporation of convection

The present approach is based on a methodology developed by Beckermann *et al.* [39] that incorporates melt convection phenomenologically in a standard phase-field model of solidification with anisotropic surface energy and kinetics. The phase-field equation is unchanged from the purely diffusive case, thus assuming that the phase field is not advected by the flow and that the phase-transition temperature does not depend on pressure. A more complete phase-field equation for the convection case, which can be reduced to a nonequilibrium form of the Clausius-Clapeyron equation, has recently been derived by Anderson *et al.* [41]. For the present purpose of studying the effects of melt convection in dendritic growth, the pressure dependence of the interface temperature can safely be neglected. The usual no-slip condition at a sharp solid-liquid interface is enforced through a varying interfacial force term in the liquid momentum equation in the diffuse interface region. The force term is chosen such that the no-slip condition is accurately reproduced regardless of the diffuse interface thickness. This is in contrast to previous approaches that treat not only the liquid but also the solid phase as Newtonian fluids and specify the viscosity of the solid phase to be much larger than that of the liquid phase [40,41]. In addition, the results of the asymptotic analysis of Karma and Rappel [4] for the purely diffusive phase-field model, which extend to the convective case [39,42], are exploited to render our computations more efficient and to investigate the limit of vanishing interface kinetics (i.e., local equilibrium at the solid-liquid interface).

Let ψ denote the phase field, where $\psi=\pm 1$ refers to the bulk solid and liquid phases, respectively. The phase field varies smoothly from 1 in the solid to -1 in the liquid in a small but numerically resolvable diffuse interface region, and the solid/liquid interface is defined by the contour $\psi=0$. The anisotropic form of the phase-field equation is given by

$$\begin{aligned}\tau(\vec{n})\partial_t\psi=&\boldsymbol{\nabla}\cdot[W^2(\vec{n})\nabla\psi]-\partial_\psi F(\psi,\lambda u)\\&+\partial_x[|\boldsymbol{\nabla}\psi|^2W(\vec{n})\partial_{\psi_x}W(\vec{n})]\\&+\partial_y[|\nabla\psi|^2W(\vec{n})\partial_{\psi_y}W(\vec{n})]\end{aligned}\tag{1}$$

and the energy equation, including the advective flux, can be written as

$$\partial_t u+(1-\phi)\vec{V}\cdot\boldsymbol{\nabla}u=D\boldsymbol{\nabla}^2u+\partial_t\phi,\tag{2}$$

where τ is a relaxation time. Both τ and W are functions of the interfacial normal $\vec{n}$ in order to account for anisotropic surface energy and kinetics. The function $F(\psi,\lambda u)=f(\psi)+\lambda u g(\psi)$ is a phenomenological free energy, where $f(\psi)=-\psi^2/2+\psi^4/4$ is a double-well function and $g(\psi)=\psi-2\psi^3/3+\psi^5/5$ is an odd function. The dimensionless temperature u is defined as $(T-T_m)/(L/C_p)$, where T_m is the

melting temperature and L and C_p are the latent and specific heat, respectively. The positive constant λ controls the coupling between the temperature field and the phase field. The interface thickness parameter W is assumed to take the form $W(\vec{n})=W_0 A_s(\vec{n})$, with

$$A_s(\vec{n})=(1-3\varepsilon)+4\varepsilon(\psi_x^4+\psi_y^4)/|\nabla\psi|^4, \tag{3}$$

where ψ_x and ψ_y are first derivatives with respect to x and y, and ε is the anisotropy strength of the surface energy. The thermal diffusivity is denoted by D, ϕ can be viewed as a solid fraction that is coupled to the phase field ψ simply by $\phi=(1+\psi)/2, \phi\in[0,1]$, and $\vec{V}$ is the intrinsic flow velocity. From the ''thin-interface'' limit analysis [4], we have the following relations that determine the relaxation time τ and coupling constant λ: $\tau=\tau_0[A_s(\vec{n})]^2$, $\lambda=a_1 W_0/d_0$, where d_0 is the capillary length, and $a_1=0.8839$ for the functional forms of $f(\psi)$ and $g(\psi)$ given above. Setting the kinetic effect to zero, as explained in Ref. [4], we have $\tau_0=a_1 a_2 (W_0)^3/(d_0 D)$, where $a_2=0.6267$ for the functional forms given above. Therefore, only W_0 is a free parameter that has to be properly selected to obtain converged solutions.

The conservation equations for mass and momentum take the following form [39]:

$$\nabla\cdot[(1-\phi)\vec{V}]=0, \tag{4}$$

$$\partial_t[(1-\phi)\vec{V}]+(1-\phi)\vec{V}\cdot\nabla\vec{V} = -(1-\phi)\nabla p/\rho+\nabla\cdot[\nu\nabla(1-\phi)\vec{V}]+\vec{M}_1^d, \tag{5}$$

where p, ρ, and ν are the pressure, density, and kinetic viscosity of the melt, respectively. The term $\vec{M}_1^d$ is a dissipative interfacial force per unit volume and is modeled as [39]

$$\vec{M}_1^d=-\nu\frac{2h\phi^2(1-\phi)}{W_0^2}\vec{V}, \tag{6}$$

where the constant h is found to be 2.757 by an asymptotic analysis of plane flow past the diffuse interface. This term serves as a distributed momentum sink in the diffuse interface region that forces the liquid velocity to zero as $\phi\to 1$ and vanishes in the bulk liquid ($\phi=0$). An important property of the interfacial force term is that the velocity profile smoothly approaches the profile for a sharp interface with a no-slip condition at $\phi=0.5$ (or $\psi=0$) regardless of the diffuse interface thickness.

B. Incorporation of thermal noise

Methods to incorporate thermal noise in the phase-field model have been developed by Karma and Rappel [43] and Pavlik and Sekerka [44]. Although some previous phase-field simulations have obtained dendritic sidebranches that resemble those observed in experiments [7], the sidebranches are generated by either numerical noise or by randomly driving the tip. In the model of Karma and Rappel, thermal noise is incorporated in a thermodynamically consistent manner using the Langevin formalism. Karma [45] has analyzed using a sharp-interface model the issue of the relative importance of the bulk and interface noises. He concluded that the interface noise drives short-wavelength interfacial fluctuations that are not selectively amplified by the morphological instability along the sides of dendrites for materials with reasonably fast attachment kinetics. This prediction was confirmed by phase-field simulations of dendritic sidebranching in two dimensions by Karma and Rappel [43], who found that the sidebranching activity remained quantitatively unchanged when phase-field simulations were carried out with (i) both the interface and bulk noises, and (ii) with only the latter. As a result, only the conserved bulk noise is considered here.

The conserved bulk noise is added to the energy conservation equation in the following manner:

$$\partial_t u+(1-\phi)(\vec{V}\cdot\nabla u=D\nabla^2 u+\partial_t\phi-\nabla\cdot\vec{q}, \tag{7}$$

where $\vec{q}$ stands for the thermal noise vector, obeying a Gaussian distribution with a variance,

$$\langle q_m(\vec{r},t)q_n(\vec{r}',t')\rangle=2Dk_B\frac{C_p T_M^2}{L^2}\delta_{mn}\delta(\vec{r}-\vec{r}')\delta(t-t'), \tag{8}$$

where k_B is the Boltzmann constant and δ is the delta function. It is helpful to express the governing equations in a dimensionless form that minimizes the number of computational parameters, and also renders the interpretation of the noise magnitude more transparent. Using W_0 as a length scale and τ_0 as a time scale, all dimensional variables are cast into their dimensionless form as $\vec{r}/W_0\to\vec{r}$, $t/\tau\to t$, $V\tau_0/W_0\to V$, $D\tau_0/(W_0)^2\to D$, $\nu\tau_0/(W_0)^2\to\nu$, $(p/\rho)(\tau_0/W_0)^2\to(p/\rho)$, and $\vec{q}\tau_0/W_0\to\vec{q}$, while W_0 and τ_0 are set to unity. The dimensionless variance of the thermal noise vector is then given by

$$\langle q_m(\vec{r},t)q_n(\vec{r}',t')\rangle=2DF_u\delta_{mn}\delta(\vec{r}-\vec{r}')\delta(t-t'), \tag{9}$$

where F_u is the magnitude of the thermal noise defined as

$$F_u=\frac{k_B T_M^2 C_p}{L^2 W_0^d}=\frac{k_B T_M^2 C_p}{L^2 d_0^d}\left(\frac{d_0}{W_0}\right)^d\equiv F_{\rm ex}\left(\frac{d_0}{W_0}\right)^d \tag{10}$$

and d is the dimension. In three dimensions, $F_{\rm ex}$ represents the magnitude of the thermal noise existing in experiments. The mean-square fluctuation of the temperature in a volume ΔV is given by $\langle\Delta T^2\rangle=k_B T_M^2/(C_p\Delta V)$, a fixed quantity for a given material. Therefore, physically $F_{\rm ex}$ can be interpreted as the mean-square fluctuation of u inside the microscopic volume $(d_0)^3$. In the present two-dimensional simulations, Eq. (10) requires for dimensional reasons L and C_p to be the latent heat of melting and the specific heat at constant pressure *per unit area*, respectively. These quantities, however, are only experimentally meaningful quantities when defined per unit volume in three dimensions. Thus, in two dimensions, $F_{\rm ex}$ can be treated as a free parameter whose value is chosen such that sidebranches form at a distance from the tip

comparable to experiment. Equation (10) then dictates how to choose F_u for a given choice of F_{ex} so as to obtain results that are independent of interface thickness. Namely, if one chooses the computational parameter (d_0/W_0) to be small compared to unity, which is the main gain in computational efficiency resulting from the reformulated asymptotics of Ref. [4], then one must scale down the magnitude of noise in the phase-field model, F_u, to keep the fluctuation strength F_{ex} constant. The main practical conclusion here is that one still has the computational freedom to choose the interface thickness if one rescales appropriately the noise strength F_u.

Because they are restricted to two dimensions, the present simulations are insufficient to address the issue of whether the strength of thermal noise present in an experiment is sufficient to produce the observed sidebranching activity. They are well suited, however, to shed light on the nontrivial effect of fluid flow on this activity and to make contact with existing sharp-interface WKB analyses of noise-induced sidebranching.

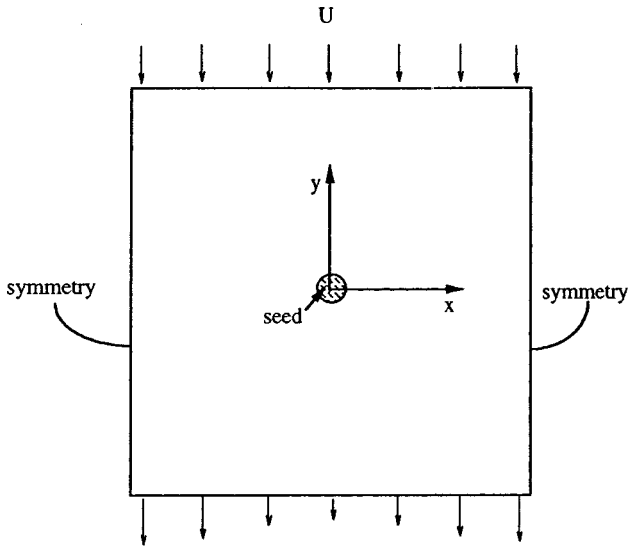

FIG. 1. Phase-field simulation domain and boundary conditions.

III. PROBLEM DESCRIPTION AND NUMERICAL PROCEDURES

The model described in the preceding section is used to numerically simulate the growth of a single dendritic crystal in a uniform forced flow. An externally forced flow was also employed in the growth experiments of Refs. [11–14], whereas the flow in other experiments [7] was buoyancy-driven. A forced flow allows for the control of the flow velocity independent of the imposed supercooling. A direct comparison of the present simulations with the forced flow experiments is, however, not possible because the simulations are limited, for computational reasons, to two dimensions and relatively large dimensionless supercoolings (see below). Instead, we focus on quantitative comparisons with analytical theories. Microscopic solvability theories of dendritic growth with melt flow are presently available only for forced convection in two dimensions.

The simulation domain is schematically illustrated in Fig. 1. A circular seed exists initially at the center of the square domain. The crystal axes are aligned with the coordinate axes, unless otherwise noted. Supercooled melt enters the domain from the top boundary with a uniform velocity U, and exits at the bottom boundary. Periodic boundary conditions are imposed on the vertical side boundaries of the domain. The initial conditions are as follows: the initial velocity field is taken to be that for steady flow around the seed, and the inlet and initial melt temperature (dimensionless) are both set to $-\Delta$ (supercooling), except inside the seed where the dimensionless temperature is zero (at the melting point). Due to the symmetry of the problem with respect to the vertical axis, simulations are carried out on only half of the domain, and the results are simply mirrored to the other half.

The mass and momentum equations are solved numerically using the multigrid SIMPLE method [46,47] on a uniform, square grid pattern. Compared to single grid methods, the multigrid method provides much stronger coupling between the pressure and velocity fields, and therefore is extremely efficient and robust when used on a highly refined grid space. The solution is first obtained on the coarsest grid using the standard SIMPLE algorithm [48]. It is then extrapolated to the next finer grid and serves as the starting solution. The solution on the second grid level is obtained using restriction and prolongation cycles [47]. This procedure continues until the solution on the finest grid level is obtained. For the results reported in this paper, we have used eight to nine grid levels. For example, starting from 5×10 control volumes (CV's), the second grid level has 10×20 CV's and the eighth grid level has 640×1280 CV's. The phase-field and energy equations were solved only on the finest grid level using an explicit Euler scheme. To take advantage of the implicit nature of the SIMPLE algorithm for the flow-field calculations, we developed a multiple time-step algorithm that uses a larger time step for the flow-field calculations while reserving a fine time step for the phase- and temperature-field calculations. The former is typically one order of magnitude larger than the latter, resulting in a roughly 60% reduction in computational time compared to using a single time step for all variables. The error in the tip velocities and radii due to this multiple time-step algorithm was found to be negligibly small. The tip radii are evaluated from the computed phase-field contours using the method explained in Ref. [4]. Finally, the generation and discretization of the conserved noise are accomplished following exactly the same procedure as Karma and Rappel in their phase-field simulations of dendritic sidebranching without flow, which is described in detail in [43].

The ranges of the governing dimensionless parameters (supercooling Δ, anisotropy strength ε, flow velocity Ud_0/D, and Prandtl number $\mathrm{Pr}=\nu/D$) considered in the present numerical simulations are strongly limited by the available computer time and memory. Since a uniform grid is used, the parameters need to be chosen such that the temperature and velocity gradients around the dendrite are accommodated in a relatively small domain in order to avoid an excessive number of grid points. Simulations are performed for dimensionless supercoolings Δ of 0.45 and 0.55 and anisotropy strengths ε ranging from 0.01 to 0.05. As

shown in previous studies that do not consider flow [4,5], these parameters allow for the choice of a relatively small domain size, while still accommodating the thermal diffusion layer around the growing dendrite. In other words, without flow, the simulation domain is chosen large enough that the dendrite tips grow in a steady state after the initial transient without being affected by the boundaries. With flow, the thermal boundary layers in front of the upward and horizontally growing dendrite tips (see Fig. 1) can be expected to be smaller than in the diffusion case. The thermal wake behind (downstream of) the crystal can become quite large, depending on the flow velocity. However, the dendrite tip in the wake grows much slower than the other ones (see below), and the thermal field is still accommodated within the domain since the crystal is placed in the center. The flow velocity is chosen small enough that the Reynolds number is less than unity. This is important for the comparison of the results with theory, as shown below. It also results in a more simple flow pattern and limits the size of the wake region. It was verified that the velocity gradients across the lower boundary (exit) are small. The Prandtl number is chosen to be equal to 23.1 in all simulations. This value is representative of SCN, a substance commonly used in dendrite growth experiments [7,13,14]. With the ratio of the velocity to thermal boundary-layer thickness approximately equal to $\mathrm{Pr}^{1/3}=2.8$, the velocity boundary layer for the upstream growing dendrite arm is still accommodated within the domain, and the upstream tip grows in a steady fashion without being affected by the boundaries. As the length of the horizontal dendrite arms increases, their growth may be influenced by the lateral boundaries, because the flow needs to be accommodated in the increasingly smaller gap between the dendrite tip and the side boundary. However, the results below show that this effect is relatively small, and the horizontal dendrite arms can grow with a relatively constant tip velocity for some time. Nonetheless, the results for the horizontal and downstream dendrite arms are not analyzed in much detail.

For steady diffusion-controlled growth ($U=0$) in two dimensions, it is possible to quantitatively benchmark the phase-field simulations using the results of microscopic solvability theory. Table I shows the present simulation results for the steady-state dendrite tip velocities and radii at a supercooling of $\Delta=0.55$ and three values of the anisotropy strength—$\varepsilon=0.01$, 0.03, and 0.05—along with the predictions of microscopic solvability theory for each case. In the table, decreasing the dimensionless thermal diffusivity D, and thus decreasing the coupling constant λ, is equivalent to decreasing the interfacial thickness. It can be seen that the phase-field results are independent of interface thickness and that quantitative agreement with the benchmark solution has been achieved.

We also numerically examined the effect of grid anisotropy by rotating the principal growth directions of a dendrite by 45°, which represents the worst scenario of grid anisotropy. For a supercooling of $\Delta=0.55$ and an anisotropy strength of $\varepsilon=0.05$, we found that the steady-state tip growth velocity for the rotated case is about 4.7% lower than for the base case. Karma and Rappel [43] proposed a method to correct for the grid anisotropy effect numerically. For example, for the grid spacing of $\Delta x/W_0=0.4$ that we have used in this study, the correction to the anisotropy strength is $(\Delta x)^2/240\cong 6.7\times 10^{-4}$, which is small compared to the nominal anisotropy strength of 0.01–0.05, so no correction is needed here. However, for a larger grid spacing, the correction will become important.

TABLE I. Phase-field simulation of dendritic growth without convection: numerical results for different diffuse interface thicknesses versus microscopic solvability theory (exact) predictions for $\Delta=0.55$. In the simulations, grid numbers are $N_x=640$ and $N_y=1280$, dimensionless spacing $\Delta x/W_0=0.4$.

D	d_0/W_0	Vd_0/D	ρ/d_0	σ^*
		$\varepsilon=5\%$		
4	0.139	0.0171	6.83	2.51
3	0.185	0.0175	6.02	3.15
2	0.277	0.0180	5.76	3.35
exact		0.0170	6.41	2.86
		$\varepsilon=3\%$		
4	0.139	0.0112	25.9	0.27
3	0.185	0.0120	24.0	0.29
2	0.277	0.0110	21.7	0.38
exact		0.0111	23.3	0.33
		$\varepsilon=1\%$		
6	0.0923	0.0036	132.2	0.032
5	0.1108	0.0041	119.0	0.034
4	0.139	0.0040	119.2	0.035
3	0.185	0.0042	117.0	0.035
exact		0.0034	129.6	0.035

IV. TIP GROWTH

A. Convection-controlled growth

Although many theories have been proposed to account for the effect of convection on dendritic growth, these theories are not rigorous because they usually prescribe a tip shape. No exact solution exists for the selection of the tip-operating state (velocity and radius) in the presence of flow. It is thus impossible to directly benchmark our numerical results, as we did for purely diffusive growth. However, the accuracy of our phase-field simulations with flow can still be established by examining their convergence behavior in the thin-interface limit. Table II summarizes the results of convergence tests for two values of the anisotropy strength. The upstream tip velocities and radii are presented for decreasing values of the diffuse interface thickness, i.e., decreasing dimensionless diffusivity D in the limit of vanishing interface kinetics, and for different grid sizes. For each anisotropy, converged results are obtained.

For a fixed supercooling of 0.55, Fig. 2 illustrates the computed evolution of the dendrites for three different anisotropy strengths ($\varepsilon=0.01$, 0.03, and 0.05) without flow (top panels) and with flow (bottom panels). For the bottom panels, the input parameters also include the flow velocity

TABLE II. Convergence study of dendritic growth with flow: results for the upstream tip steady-state velocity V and radius ρ for different grids and diffuse interface thicknesses. In the simulations, the following parameters were held constant: supercooling $\Delta=0.55$, Prandtl number Pr=23.1, and $\Delta x/W_0=0.4$. T_{CPU} denotes the CPU time in hours on a HP C200 workstation; N_x and N_y are the number of control volumes in the x and y directions, respectively.

ε	Ud_0/D	D	d_0/W_0	N_x	N_y	Vd_0/D	ρ/d_0	T_{CPU}
0.03	0.135	3	0.185	640	1280	0.0288	16.8	45
0.03	0.135	2	0.277	640	1280	0.0296	15.5	60
0.03	0.135	1	0.554	1024	2048	0.0303	14.7	150
0.03	0.135	2	0.277	1024	2048	0.0286	14.9	120
0.05	0.035	4	0.139	160	320	0.0265	8.10	3
0.05	0.035	4	0.139	288	576	0.0240	7.51	8
0.05	0.035	4	0.139	576	1152	0.0244	7.46	31
0.05	0.035	3	0.185	320	640	0.0248	7.48	17
0.05	0.035	2	0.277	512	1024	0.0247	7.61	70

$Ud_0/D=0.07$ and the Prandtl number $\mathrm{Pr}=\nu/D=23.1$. These calculations were performed on a grid of 320×640 CV's with a uniform spacing of $\Delta x/W_0=0.4$. For better visualization, we have interpolated the flow field onto a grid that is about 60 times coarser than the one used in the computations. It can be seen that the shape of the dendrites is significantly influenced by the flow. The growth velocities of the upstream tips are much higher than those of the downstream tips and the tips normal to the flow, because the impinging flow reduces the thermal boundary-layer thickness on the upstream side. The evolution of the downstream arm in the wake of the dendrite is retarded relative to even the diffusion case, because of advection of heat from the upstream portion of the dendrite. An interesting observation is that the horizontal tips grow slightly upwards. This dendrite ''tilting'' is due to the asymmetry of the heat fluxes on the upper and lower sides of the horizontal arm.

Figure 3(a) shows the evolution of all tip velocities (upstream, normal to flow, and downstream) for the following example: $\Delta=0.55$, $\varepsilon=0.03$, $Ud_0/D=0.135$, and Pr $=23.1$. For comparison, the value of the steady growth velocity in the absence of flow is also plotted. All tip velocities start from a large value before leveling off. This initial decrease is simply caused by the initial conditions. The upstream tip eventually reaches a steady state with a growth speed that is about 160% higher than the value in the absence of flow. The tip that grows in a horizontal direction normal to the flow appears to slow down even after a long time, although the decrease after about $t/\tau=400$ is very small. The average growth speed for $800<t/\tau<1000$ is only about 20% higher than the pure diffusion value. Note that the flow past the horizontal tip continually accelerates because the inlet mass flow rate has to be accommodated in an increasingly smaller gap between the tip and the side boundary. The downstream tip also does not reach a complete steady state due to the ever-increasing size of the dendrite, but a similar average shows that its speed is approximately 45% lower than without flow. Figure 3(b) shows the evolution of the tip radii corresponding to the conditions of Fig. 3(a). Again the upstream tip reaches a steady-state radius (about 35% lower than the no-flow value), while the other tips continue to evolve slowly.

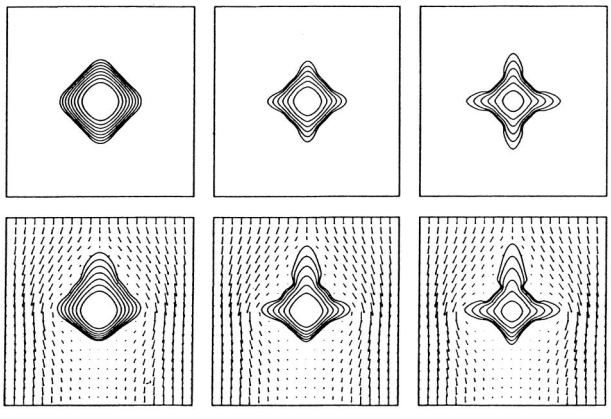

FIG. 2. Evolution of phase-field contours for a dendrite growing at $\Delta=0.55$ and $\varepsilon=0.01$, 0.03, and 0.05 (from left to right) without convection (top panels) and with convection (bottom panels) for a flow velocity of $Ud_0/D=0.7$ and a Prandtl number of Pr=23.1 (320×640 CV's with a uniform spacing of $\Delta x/W_0=0.4$).

The knowledge of the tip velocity and radius allows for the calculation of two important parameters in dendritic growth: the tip growth Peclet number, $\mathrm{Pe}\equiv V\rho/(2D)$, and the selection constant, σ^*, defined by $\rho^2V\equiv2d_0D/\sigma^*$. For the example shown in Fig. 3, we find $\mathrm{Pe}\cong0.21$,$\sigma^*\cong0.30$ for the upstream tip; $\mathrm{Pe}\cong0.14$,$\sigma^*\cong0.36$ for the tip normal to the flow; and $\mathrm{Pe}\cong0.09$,$\sigma^*\cong0.38$ for the downstream tip. For the same supercooling and anisotropy strength but without flow, we have $\mathrm{Pe}\cong0.12$,$\sigma^*\cong0.39$. The differences in the Peclet numbers simply reflect the effect of the flow on the heat transfer at the differently oriented tips. The fact that the convection value of σ^* for the horizontally growing tip is close to the diffusion value is in agreement with the experiments of Bouissou *et al.* [11], who found that σ^* does not depend on the transverse component of the flow. The fact that the downstream tip also has a σ^* value close to the diffusion value may be explained by the relative weakness of the flow in the wake region of the dendrite. On the other hand, the upstream tip for the example of Fig. 3 has a σ^* value that is significantly different from the no-flow case. This issue is

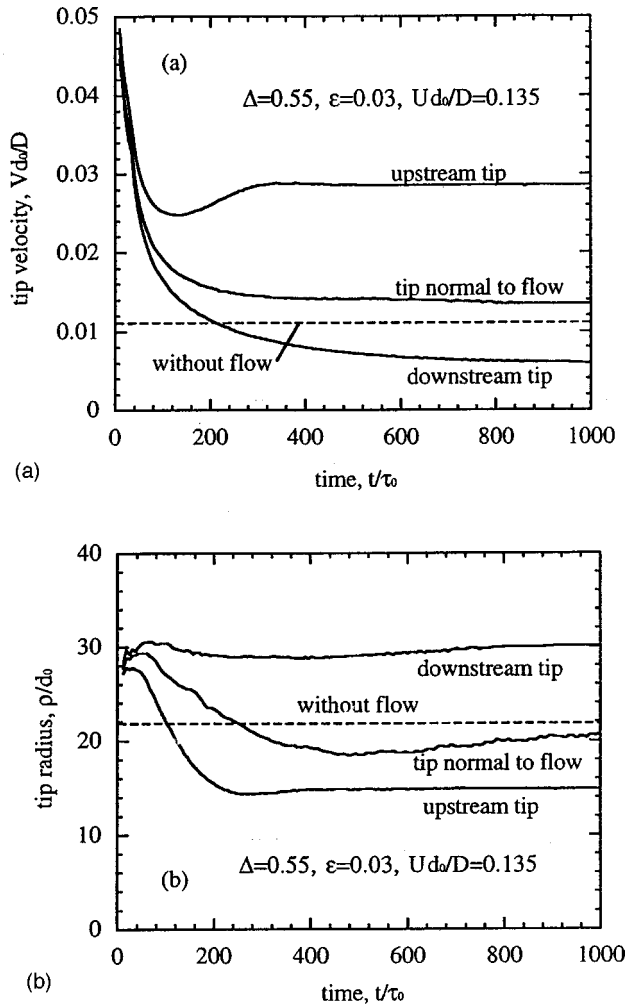

FIG. 3. The operating state of dendrite tips in a forced flow for the case of $\Delta=0.55$, $\varepsilon=0.03$, $Ud_0/D=0.135$, and $\mathrm{Pr}=23.1$. (a) Evolution of dendrite tip velocities; (b) evolution of dendrite tip radii.

investigated in more detail in the following by comparing the present results for the upstream tip to the linearized solvability theory of Bouissou and Pelce [23] for dendrite growth with a uniform axial flow from a direction opposite to the growth direction.

B. Comparison with linearized solvability theory

Bouissou and Pelce [23] studied theoretically the effect of a forced flow on the operating state of a dendrite tip in two dimensions. Their theory consists of two parts: the heat transport solution and the linearized solvability analysis. The flow is assumed to be in the small Reynolds number regime where the Oseen flow approximation is valid. In that regime, the nonlinear convective terms in the Navier-Stokes equations can be linearized to yield the well-known Oseen equations. By assuming the dendrite tip shape to be parabolic and the surface energy to be negligible, they obtained a relationship between the growth Peclet number (Pe_c), flow Peclet number (Pe_f), and the supercooling (Δ),

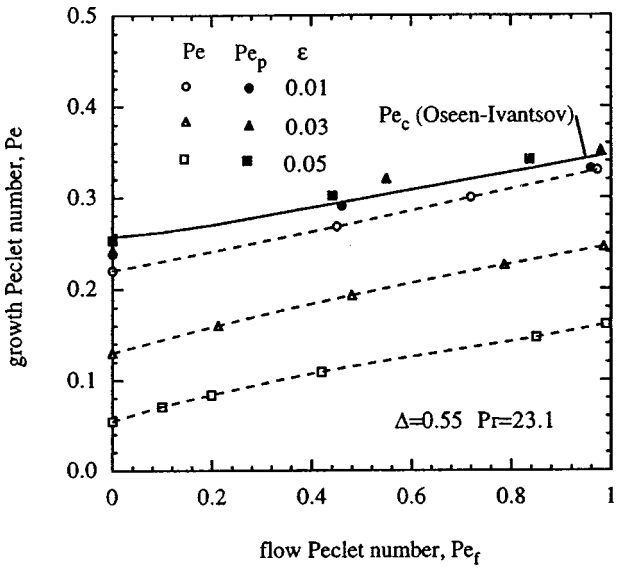

FIG. 4. Variations of the growth Peclet number with the flow Peclet number, and comparison with the two-dimensional Oseen-Ivantsov solution (solid line) for $\Delta=0.55$ and $\mathrm{Pr}=23.1$. Both the growth and flow Peclet numbers are evaluated using the actual tip radius ρ for the open symbols and dashed lines, and the radius ρ_p based on the parabolic fit for the solid symbols.

$$\Delta=\mathrm{Pe}_c\exp(\mathrm{Pe}_c-\mathrm{Pe}_f)\int_1^\infty\frac{d\eta}{\sqrt{\eta}}\times\left\{-\mathrm{Pe}_c\eta+\mathrm{Pe}_f\left(2+\int_1^\eta\frac{g(\zeta)}{\sqrt{\zeta}}d\zeta-\eta\right)\right\},\quad(11)$$

where $\mathrm{Pe}_f\equiv U\rho/(2D)$ is the flow Peclet number, and the subscript c on the growth Peclet number serves to distinguish it from the Peclet number obtained from simulation. The function $g(\zeta)$ is defined as

$$g(\zeta)=\sqrt{\zeta}\frac{\mathrm{erfc}(\sqrt{\mathrm{Re}\,\zeta/2})}{\mathrm{erfc}(\sqrt{\mathrm{Re}/2})}+\frac{\sqrt{2/(\pi\,\mathrm{Re})}}{\mathrm{erfc}(\sqrt{\mathrm{Re}/2})}\{\exp(-\mathrm{Re}/2)-\exp(-\mathrm{Re}\,\zeta/2)\},\quad(12)$$

where $\mathrm{Re}\equiv U\rho/\nu=2\,\mathrm{Pe}_f/\mathrm{Pr}$ is the Reynolds number. It is important to note that Eqs. (11) and (12) apply only to the upstream tip in the present simulations. The relationship $\Delta=\Delta(\mathrm{Pe}_c,\mathrm{Pe}_f)$ reduces to the well-known two-dimensional Ivantsov solution in the absence of flow ($\mathrm{Pe}_f=0$). A heat transport solution of the same type, although written in a different form, has also been derived by Ananth and Gill [19].

The upstream tip Peclet numbers extracted from the simulations are compared to the predicted values (Pe_c) from the Oseen-Ivantsov relation [Eq. (11)] in Fig. 4 for $\Delta=0.55$, $\mathrm{Pr}=23.1$, with Pe_f ranging from 0 to 1($\mathrm{Re}<0.1$), and three anisotropy strengths ($\varepsilon=0.01$, 0.03, and 0.05). While the Peclet numbers increase with increasing flow velocity, the ones from the simulations are significantly below the predictions from the Oseen-Ivantsov relation, with the gap between

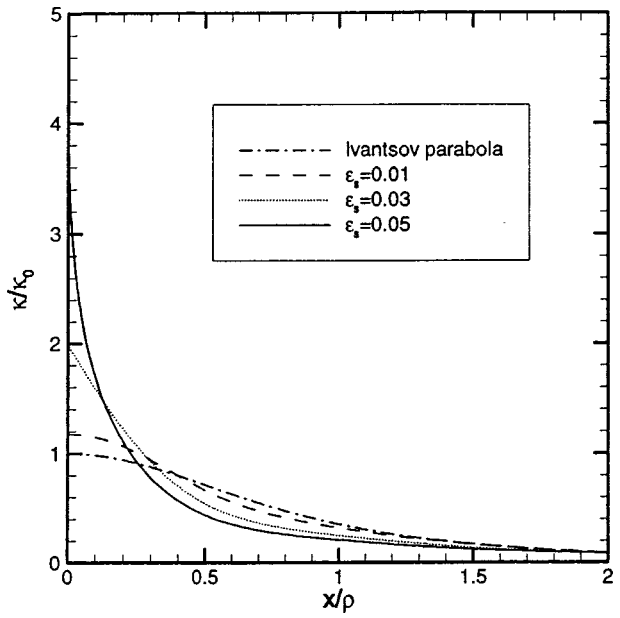

FIG. 5. Curvature variation along a needle crystal as a function of surface energy anisotropy (zero anisotropy represents the Ivantsov parabola).

simulation and theory increasing with ε. This gap has been observed previously in a purely diffusive regime [4,36]. It is due to the fact that the interface shape deviates from a parabola close to the tip, with this deviation increasing steeply with anisotropy strength.

The phase-field calculations enable us to quantitatively examine the deviation of the computed tip shape from the parabolic shape assumed in the theory. A parabola can be expressed as

$$x^2 = -2\rho_0 z \quad \text{or} \quad (x/\rho_0)^2 = -2z/\rho_0, \tag{13}$$

where the origin of the coordinates (x-z) is located at the tip, with the z axis pointing at the growth direction of the dendrite and the x axis perpendicular to the growth axis, and ρ_0 is the tip radius of the parabola. The curvature of the parabola varies with x as

$$\frac{\kappa}{\kappa_0} = \frac{1}{[1+(x/\rho_0)^2]^{3/2}}, \tag{14}$$

where $\kappa_0 = 1/\rho_0$ is the curvature of the tip. Figure 5 shows a comparison of the curvature variation of the parabola from Eq. (14) with the curvatures measured from phase-field simulations in the absence of convection for three anisotropy strengths (0.01, 0.03, and 0.05). It is seen that for $\varepsilon = 0.05$, the curvature at the tip ($x/\rho = 0$) is almost four times larger than that of a parabola. However, for the lowest anisotropy (0.01), the tip shape is reasonably close to a parabola. All curvatures become almost identical after about $x/\rho = 1.5$. This implies that the anisotropy influences the dendrite shape only in the region very close to the tip. Farther away from the tip, the interface shape is accurately fitted by a parabola, $z = -x^2/2\rho_p$.

Consequently, in order to meaningfully compare our results to the predictions of the Oseen-Ivantsov relation, which is based on a parabolic tip shape, we must use the fitted radius ρ_p instead of the actual radius ρ when calculating the tip Peclet number for our simulations. For this purpose, we extracted the parabolic tip radius, ρ_p, by measuring the slope of z versus x^2 in the region of the simulated interfaces behind the tip where this plot becomes a straight line. Note that ρ_p is likely to be the experimentally measured tip radius since a parabolic fit of the tip shape has been traditionally used to extract this parameter, even though it does not correspond to the actual tip radius. Using ρ_p and the tip velocity V from our simulations, we calculated a parabolic Peclet number, $\mathrm{Pe}_p = V\rho_p/2D$, and for later use the parabolic selection parameter, $(\sigma^*)_p = 2Dd_0/(\rho_p^2 V)$. As opposed to Pe, Pe_p is in good agreement with Pe_c predicted from Eq. (12) for all flow and anisotropy strengths, as shown in Fig. 4.

The linear solvability analysis by Bouissou and Pelce [23] reveals that the ratio of the selection parameters without flow and with flow is a function of a dimensionless flow parameter χ,

$$\chi = a(\mathrm{Re})d_0 U/(\beta^{3/4}\rho V), \tag{15}$$

where $\beta = 15\varepsilon$ and $a(\mathrm{Re})$ is given by

$$a(\mathrm{Re}) = \sqrt{2\,\mathrm{Re}/\pi}\,\exp(-\mathrm{Re}/2)/\mathrm{erfc}(\sqrt{\mathrm{Re}/2}). \tag{16}$$

For $\chi > \chi_c$, where χ_c is a critical threshold value much larger than unity, the following asymptotic form holds:

$$(\sigma^*)_0/\sigma^* \cong 1 + b\chi^{11/14}, \tag{17}$$

where $(\sigma^*)_0$ is the selection parameter without flow and b is a constant. For χ smaller than unity, which is the case in the present simulations, the ratio of selection parameters is independent of the flow parameter, i.e.,

$$(\sigma^*)_0/\sigma^* \cong 1. \tag{18}$$

We verified and refined the latter prediction by numerically evaluating the complex solvability integral derived by Bouissou and Pelce [23], and found that the ratio increases by about 1% over the range of $0 < \chi < 0.2$, which corresponds to the present simulations. Physically, the analysis of Bouissou and Pelce implies that flow has an effect on the tip-selection parameter only if $(d_0 U)/(\rho V) = \mathrm{Pe}_f \sigma^*$ is of the order of unity or greater.

Figure 6 shows that the ratio $(\sigma_p^*)_0/(\sigma_p^*)$ of parabolic selection parameters without and with flow is indeed nearly independent of the flow parameter for all ε and Δ, in agreement with the linear solvability theory prediction. The applicability of this theory, which assumes a purely parabolic tip, may seem surprising. We note, however, that this nontrivial feature of the linearized solvability theory is already present without flow. In this case, the theory predicts reasonably well the tip velocity over a comparable range of anisotropy in both two [49] and three [50] dimensions despite the presence of a localized tip distortion that causes ρ to depart from ρ_p. Thus, we can conclude that even in the presence of flow, this

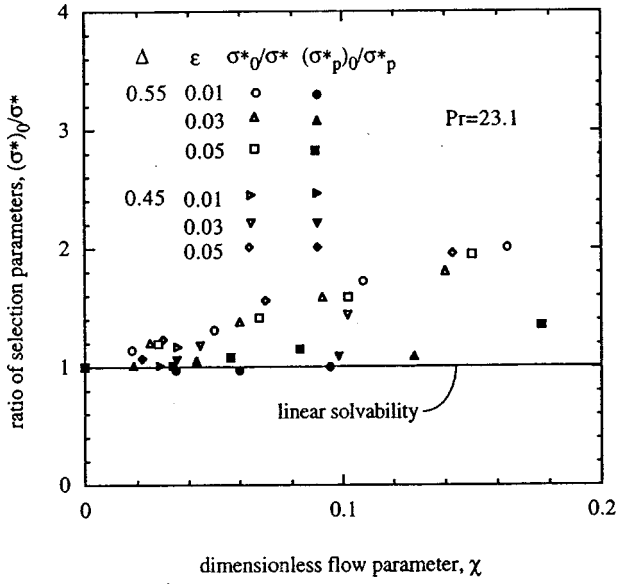

FIG. 6. Variation of the ratio of the selection parameters without and with flow as a function of the dimensionless flow parameter χ and comparison with the linear solvability theory for a parabolic tip (the theoretical lines for all three anisotropy strengths coincide). Both the ratio of the selection parameters and the flow parameter are evaluated using the actual tip radius ρ for the open symbols and the radius ρ_p based on the parabolic fit for the solid symbols.

distortion does not strongly affect the selection of the tip velocity and the two-dimensional parabolic tip shape on a larger scale of ten tip radii.

In contrast, Fig. 6 also shows that the ratio of selection parameters based on the actual tip radius varies by a factor of up to about 2 over the range of flow velocities investigated, even though χ is small. This result shows that the advection of heat by the flow has a strong effect on the portion of the dendrite shape within about one tip radius of the tip, which is controlled in the absence of flow by the balance between anisotropic surface tension and diffusion. It is presently not clear why all results for the ratio of selection parameters based on the actual tip radius, $(\sigma^*)_0/(\sigma^*)$, appear to fall along a single line in Fig. 6. This would indicate that χ remains a useful scaling parameter even when using the actual tip radius. Certainly, the variation of $(\sigma^*)_0/(\sigma^*)$ in Fig. 6 should not be construed as a test of the solvability result given by Eq. (17).

V. SIDEBRANCHING

A. Sidebranching with convection

The flow influences not only the tip-operating state, as discussed in the preceding section, but also the dynamics of dendritic sidebranching. In the following, we will study the dynamics of sidebranching by presenting simulation results for different flow velocities, thermal noise strengths, and flow directions relative to the growth axes. The following parameters are held constant: supercooling $\Delta=0.55$, anisotropy strength $\varepsilon=3\%$, and Prandtl number $\mathrm{Pr}=23.1$. Without flow, the tip-operating state is given by $Vd_0/D\cong 0.011$, $\rho/d_0\cong 21.8$, and $\sigma^*\cong 0.38$. All calculations in this section were performed on a grid of 1024×2048 CV's with a uniform spacing of $\Delta x/W_0=0.4$.

Simulation results for a noise strength of $F_u=1.25\times 10^{-4}$ and a flow velocity of $Ud_0/D=0.027$ are shown in Fig. 7. For these conditions, the steady-state operating state of the upstream tip is evaluated as $Vd_0/D\cong 0.0164$, $\rho/d_0\cong 18.5$, and $\sigma^*\cong 0.36$. Figure 7(a) shows the computed evolution of the phase-field contours from time $t/\tau_0=4500$ to 6000, in equal time intervals of 300, together with the velocity vectors at $t/\tau_0=6000$. It can be seen that the upstream arm develops numerous sidebranches, whereas the horizontal and downstream arms are just beginning to show instabilities. Figure 7(b) shows the isotherms at $t/\tau_0=5850$. The temperature fluctuations are reflected by the noisiness of the contours. In order to analyze the amplitude and wavelength of the sidebranches in more detail, the temporal variation of the half-width $x=x(z,t)$ of the upstream growing dendrite arm is plotted in Fig. 7(c) for three locations behind the tip ($|z|/\rho=20$, 40.5, and 61). These results are analyzed in the next section.

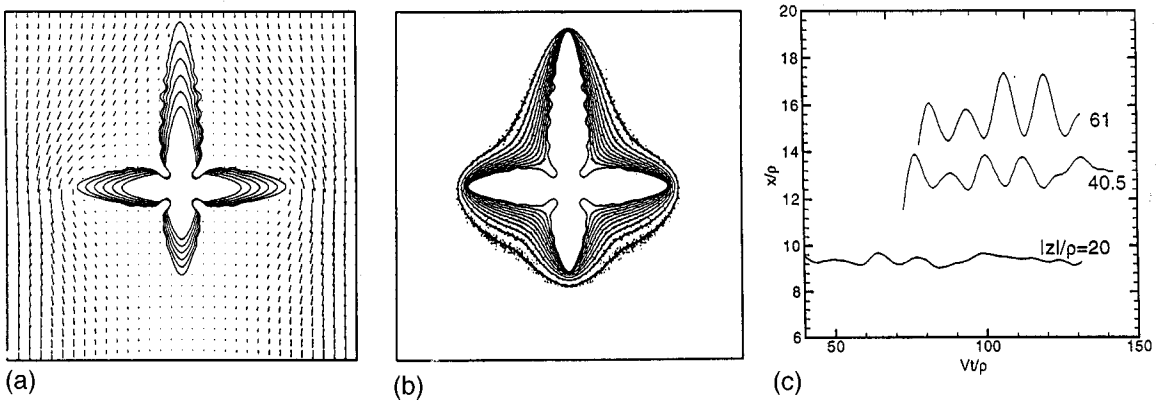

FIG. 7. Dendritic sidebranching in a forced flow ($Ud_0/D=0.027$, $F_u=1.25\times 10^{-4}$, $\mathrm{Pr}=23.1$, $\Delta=0.55$, and $\varepsilon=0.03$). (a) Morphological development from $t/\tau_0=4500$ to 6000 in equal time intervals of 300; (b) isotherms around the growing dendrite at $t/\tau_0=5850$; (c) spectra of sidebranches at three locations behind the tip.

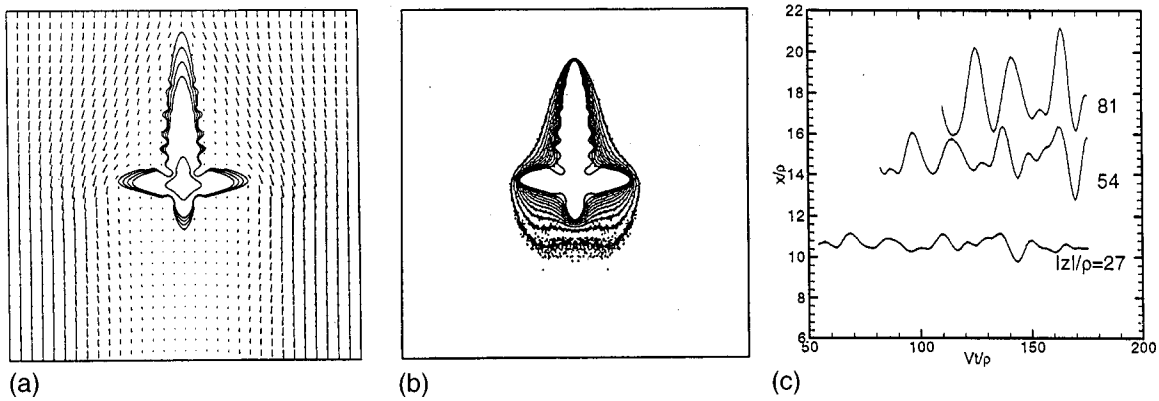

FIG. 8. Dendritic sidebranching in a stronger forced flow ($Ud_0/D=0.135$) compared to Fig. 7. (a) Morphological development at $t/\tau_0=1050$ and 2550 to 3450 in equal time intervals of 300; (b) isotherms around the growing dendrite at $t/\tau_0=2850$; (c) spectra of sidebranches at three locations behind the tip.

Figure 8 shows simulation results for a case in which the flow velocity is five times larger (i.e., $Ud_0/D=0.135$) than in the case corresponding to Fig. 7. The phase-field contours in Fig. 8(a) correspond to $t/\tau_0=1050$, 2550, 2850, 3150, and 3450. These times are smaller than in Fig. 7(a) because the upstream dendrite arm grows much faster, while the size of the computational domain is unchanged. Since the horizontal arms grow at approximately the same velocity in Figs. 7 and 8, they can serve as a convenient length scale when comparing the two figures.

Figure 9 shows the simulation results for a case in which the noise strength was increased by a factor of 4 relative to the cases of Figs. 7 and 8 (to $F_u=5\times10^{-4}$), while the flow velocity is the same as in Fig. 8. In Fig. 9(a), the phase-field contours are plotted from $t/\tau_0=2400$ to 3300, in equal intervals of 300. As expected, the amplitude of the sidebranches on the upstream growing dendrite arm increases substantially compared to Fig. 8. The isotherms shown in Fig. 9(b) for $t/\tau_0=3300$ are also considerably more noisy than in Fig. 8(b). These results are in qualitative agreement with the experimental study by Bouissou *et al.* [30] on pivalic acid (PVA) dendrites. They found that the amplitude of the sidebranches increases with the amplitude of the external perturbations in the ''linear regime'' close to the tip. A comparison with noise amplification theory is made in the next section.

The flow field around a growing two-dimensional, sidebranching dendrite is interesting and deserves further discussion. The vector plots of Figs. 7(a), 8(a), and 9(a) show the actual magnitude of the velocities, but are too coarse to resolve all flow patterns. Figure 10 shows an example of computed streamlines at two different times. The contours are plotted at unequal intervals in order to illustrate better the weaker flows around the dendrite. At the early time [Fig. 10(a)], the flow pattern is similar to low Reynolds number cross flow around a circular cylinder and there is no boundary-layer separation in the wake region. When the flow velocity or the dendrite size is large enough, boundary-layer separation occurs in the wake region, as shown in Fig. 10(b). Two relatively weak recirculation cells exist on the downstream side of the horizontal arms, and the melt actually flows toward the downward growing tip. This is reflected by the isotherms in Figs. 8(b) and 9(b), which show an inflection in front of the downward growing tip.

A direct illustration of the effect of convection on the upstream growing dendrite arm is provided in Fig. 11, where each panel is a snapshot of the phase-field contours of the

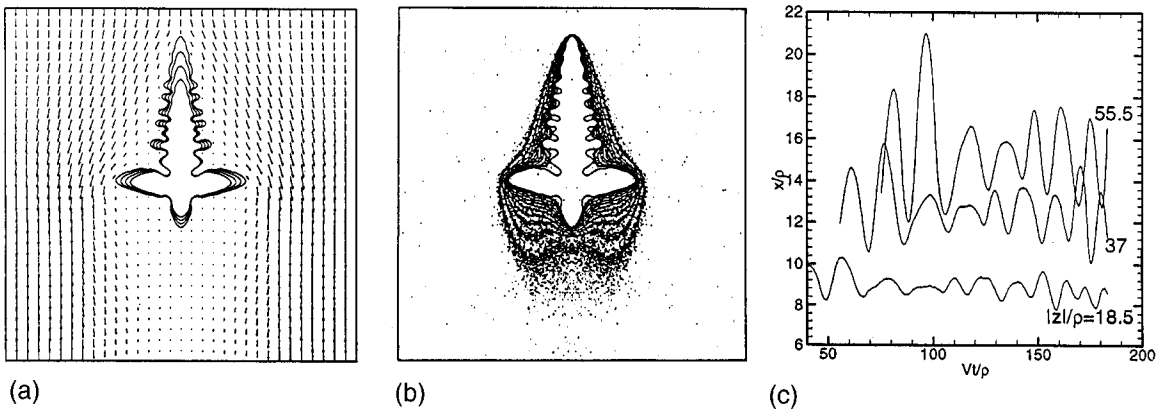

FIG. 9. Dendritic sidebranching with a larger noise strength ($F_u=5\times10^{-4}$) compared to Fig. 8. (a) Morphological development from $t/\tau_0=2400$ to 3300 in equal time intervals of 300; (b) isotherms around the growing dendrite at $t/\tau_0=3300$; (c) spectra of sidebranches at three locations behind the tip.

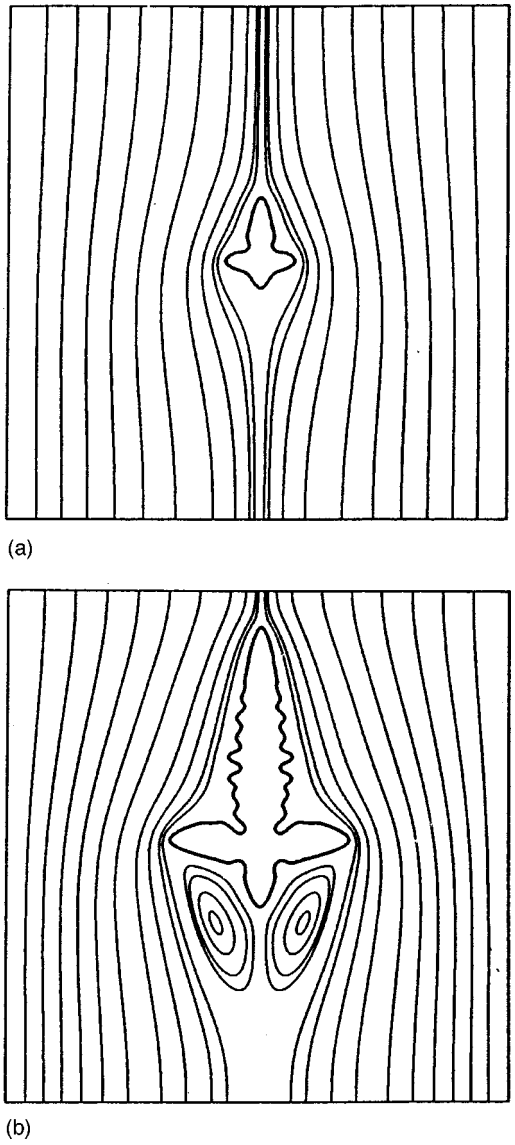

FIG. 10. Flow field around a growing dendrite ($Ud_0/D=0.135$, $F_u=1.25\times10^{-4}$, Pr=23.1, $\Delta=0.55$, and $\varepsilon=0.03$). (a) When the dendrite is small ($t/\tau_0=900$), there is no boundary-layer separation in the wake region; (b) when the dendrite becomes larger ($t/\tau_0=3450$), two symmetric recirculation cells appear in the wake region.

arm during the steady-state growth regime. In both Figs. 11(a) (upper panels) and 11(b) (lower panels), the melt velocity increases from $Ud_0/D=0$ (purely diffusive) for the left panel, over 0.027 for the middle panel, to 0.135 for the right panel. All other parameters, including the noise level (at $F_u=1.25\times10^{-4}$), are held constant. In Fig. 11(a) (upper panels), the coordinates are unscaled, i.e., the images are of equal magnification. It can be seen that sidebranching is enhanced with increasing flow velocity, and both the amplitude and frequency of the sidebranches increase from left to right. On the other hand, the primary tip radius decreases with increasing flow velocity. The tip radii (ρ/d_0) are measured to be 21.8, 18.5, and 14.9 for the flow velocities of $Ud_0/D=0$, 0.027, and 0.135, respectively, corresponding to the three panels of Fig. 11(a). Using these tip radii as length scales to normalize the coordinates, the three panels of Fig. 11(a) are replotted in Fig. 11(b). Other than for the random nature of the instabilities, the frequency of the sidebranches now appears virtually the same for all three cases. The sidebranch amplitude may be slightly increasing with flow velocity, but a definite conclusion is difficult to extract from Fig. 11(b). The fact that the sidebranch wavelength scales with the tip radius in the presence of flow is qualitatively consistent with the scaling law $\langle\lambda\rangle/\rho=\text{const}$, where $\langle\lambda\rangle$ is some mean sidebranch wavelength, observed in the classical experiments of Huang and Glicksman [7]. Although Huang and Glicksman varied only the supercooling, the melt velocities changed substantially in their experiments because the intensity of natural convection changes with supercooling.

The effect of different thermal noise strengths in the presence of flow is examined in more detail in Fig. 12, which shows snapshots of upstream growing arms similar to Fig. 11. The higher noise level (5×10^{-4}, right panel) clearly results in a larger sidebranch amplitude compared to the lower noise level (1.25×10^{-4}, left panel). However, the wavelength of the sidebranches appears to be unchanged. This observation is consistent with classical noise amplification theory. A more quantitative comparison with linear WKB theory is presented in the next section.

In order to investigate the influence of the flow direction relative to the growth direction on the dynamics of dendritic sidebranching, we performed a simulation in which the crystal axes are set at an angle of 45° with respect to the flow. Figure 13 shows the computed phase-field contour at $t/\tau_0=3540$ for a noise strength of $F_u=1.25\times10^{-4}$ and a flow velocity of $Ud_0/D=0.135$. A simulation result without noise (dotted line in Fig. 13) is also included for comparison. Under these conditions, the steady-state operating state for the dendrite arm growing into the upper right corner is given by $Vd_0/D\cong0.023$, $\rho/d_0\cong15.5$, and $\sigma^*\cong0.36$. It can be seen from Fig. 13 that the shape and sidebranching behaviors are significantly influenced by the flow direction. Compared to an upstream arm growing directly into the flow [Fig. 8(a)], the growth of the 45° arm demonstrates a strong asymmetric behavior. The sidebranching is much more developed on the upper side than on the lower side of the arm. An asymmetric behavior can also be observed in the no-noise case (dashed line), where the growth is promoted on the upper side by the flow while it is suppressed on the lower side. This results in an asymmetric needle crystal with the upper half of the crystal (divided by the growth axis) much wider than the lower half of the crystal. Obviously, this asymmetry is caused by the flow inducing a higher heat flux on the upper side of the dendrite arm and advecting heat around the arm that suppresses growth on the lower side. The asymmetry in the growth results in a slight dendrite ''tilting'' phenomenon for the 45° growing arm. At $t/\tau_0=3540$ (Fig. 13), the growth axis, defined as a straight line between the center of the crystal and the tip of the arm, is at an angle of 42.5° with respect to the vertical, indicating a 2.5° upward tilt.

B. Comparison with linear WKB theory

Figures 7(c), 8(c), and 9(c) show the numerically calculated temporal variation of the half-width of the upstream

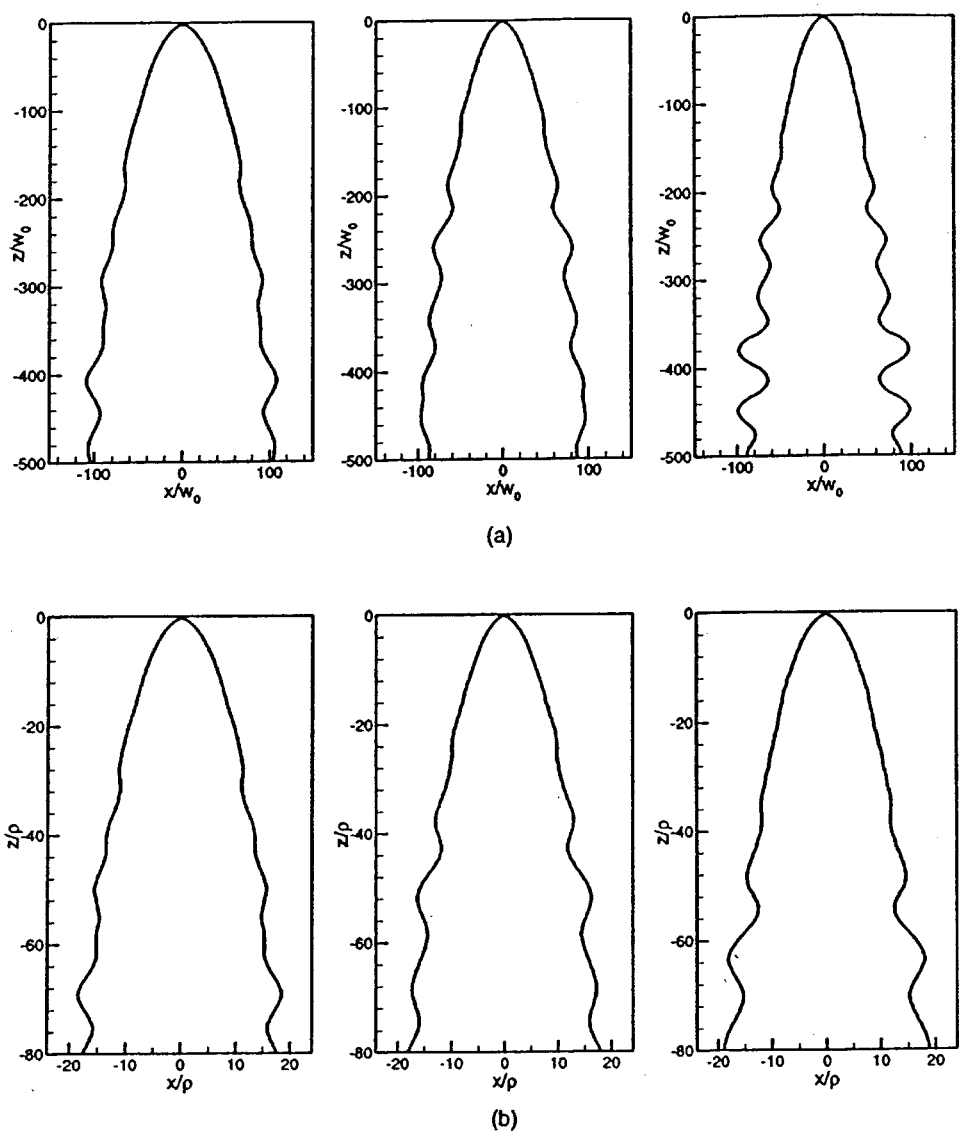

FIG. 11. Effect of flow on dendritic sidebranching. (a) Unscaled snapshots of the upstream growing dendrite arm; (b) snapshots of the upstream growing dendrite arm scaled with the tip radius. From left to right, flow velocity is increased from $Ud_0/D=0.0$ and 0.027 to 0.135. Other input parameters are kept constant at $\Delta=0.55$, $\varepsilon=0.03$, Pr=23.1, and $F_u=1.25\times10^{-4}$.

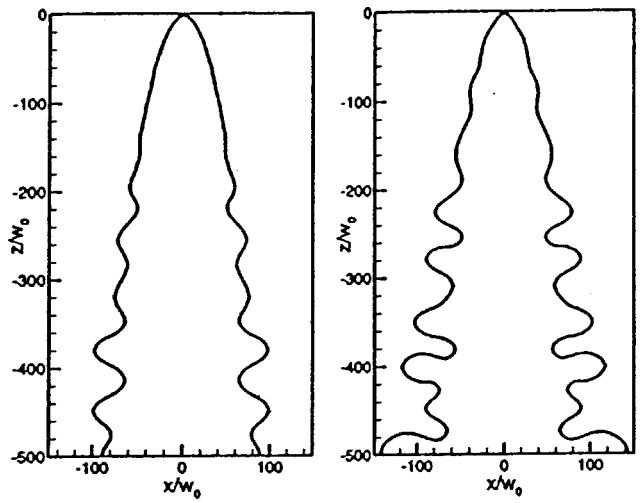

FIG. 12. Snapshots of the upstream growing dendrite arm at two noise levels, $F_u=1.25\times10^{-4}$ and 5×10^{-4}. Other input parameters are kept constant at $Ud_0/D=0.135$, Pr=23.1, $\Delta=0.55$, Pr=23.1, and $\varepsilon=0.03$.

growing dendrite arm at several fixed positions behind the tip. Each oscillation corresponds to a sidebranch passing by the observation point. Statistical analysis of the spectra in these figures yields two quantities, the root-mean-square amplitude A and the mean wavelength $\langle\lambda\rangle$ as a function of distance z from the tip, that can be compared to theory. The root-mean-square amplitude $A(z)$ is defined as [43]

$$A(z)=\sqrt{\langle[x(z,t)-x_0(z)]^2\rangle}, \tag{19}$$

where $x_0(z)$ is the steady-state position of the interface in the absence of thermal noise, which was obtained by time-averaging the spectrum $x(z,t)$ shown in Figs. 7(c), 8(c), and 9(c). The mean wavelength $\langle\lambda\rangle$ is defined as

$$\langle\lambda(z)\rangle=2V(t_2-t_1)/N(z), \tag{20}$$

where $N(z)$ refers to the number of extrema of $x(z,t)$ in a time interval $[t_1,t_2]$. Equations (19) and (20) allow for the

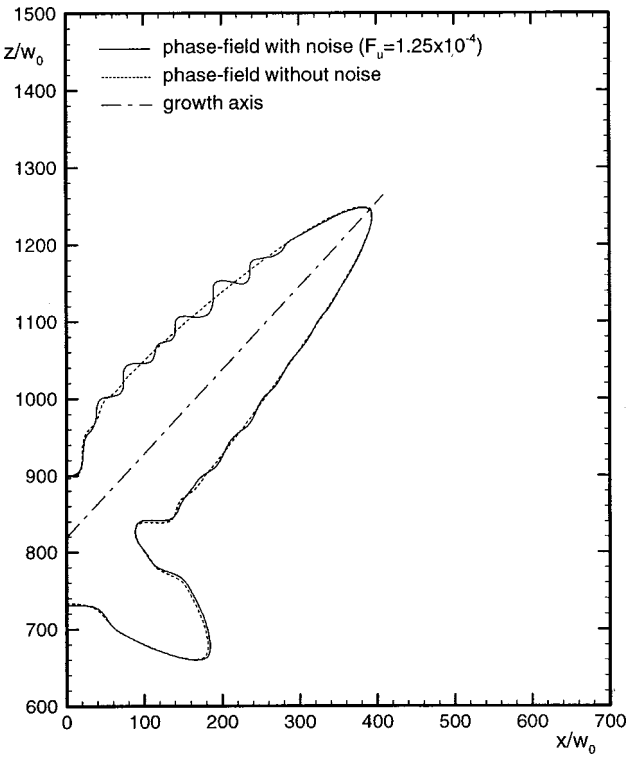

FIG. 13. Sidebranching for a dendrite with the crystal axes oriented at 45° with respect to the flow at $t/\tau_0=3540$ ($Ud_0/D=0.135$, $F_u=1.25\times10^{-4}$, Pr=23.1, $\Delta=0.55$, and $\varepsilon=0.03$). The dotted line represents the corresponding needle crystal obtained by phase-field simulation without noise. The growth axis of the arm growing into the upper right corner (dotted-dashed line) is at an angle of 42.5° with respect to the vertical.

measurement of the amplitudes and wavelengths from the phase-field results with thermal noise at various distances from the tip.

Langer [27] and Brener and Temkin [28] have theoretically analyzed noise-induced sidebranching for specific three-dimensional needle crystal shapes (a parabola of revolution, $x_0\sim z^{1/2}$, and a nonaxisymmetric dendrite with a power law for the ridges, $x_0\sim z^{3/5}$, respectively) using the WKB approximation. Good agreement with experimental data on the growth of dendrite sidebranches was found for the nonaxisymmetric needle crystal shape of Brener and Temkin. Karma and Rappel [43] have extended the above analyses to arbitrary needle crystal shapes $x=x_0(z)$ in two or three dimensions, allowing for a direct comparison with the phase-field results using computed noiseless interface shapes. By considering the stability analysis of Bouissou and Pelce [23], we found that the WKB sidebranching relations derived by Karma and Rappel [43] remain unchanged in the presence of an external axial flow. This can be seen from the dispersion relation provided as Eq. (30) in Ref. [23], where the term accounting for the modification of the advection of the perturbations along the crystal by the external flow is proportional to the cosine of the angle between the normal to the interface and the growth axis. Since this angle is close to 90° far from the tip in the region where sidebranching takes place, the flow effect becomes negligibly small. Therefore,

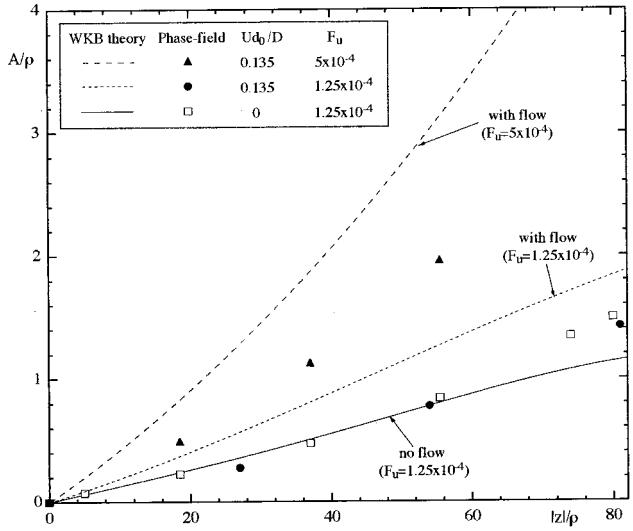

FIG. 14. Calculated sidebranch amplitudes for the upstream growing dendrite arm without and with flow ($Ud_0/D=0.135$) and two noise strengths ($F_u=1.25\times10^{-4}$ and 5×10^{-4}) as a function of distance behind the tip for $\Delta=0.55$, $\varepsilon=0.03$, and Pr=23.1. The corresponding WKB predictions are plotted as different lines.

the final expressions for the sidebranch amplitude and wavelength variations with distance from the tip valid both with and without flow are given, respectively, by

$$\frac{A(z)}{\rho}=\overline{S}\exp\left[\frac{2}{3}\left(\frac{\overline{x}_0^3}{3\sigma^*\overline{z}}\right)^{1/2}\right], \tag{21}$$

$$\frac{\langle\lambda(z)\rangle}{\rho}=\pi\left[\frac{12\sigma^*\overline{z}}{\overline{x}_0}\right]^{1/2}, \tag{22}$$

where $\overline{x}_0=x_0/\rho$ and $\overline{z}=-z/\rho$ are the coordinates of the needle crystal scaled with the tip radius. The quantity $\overline{S}$ denotes the dimensionless amplitude of the thermal noise, and is given by [43]

$$\overline{S^2}=\frac{2F_uD}{\rho^{1+d}V}=\frac{2F_u}{\tilde{d}_0^d\tilde{\rho}^{1+d}\tilde{V}}, \tag{23}$$

where $d=2$ for two dimensions and $d=3$ for three dimensions, $\tilde{V}=Vd_0/D$, $\tilde{\rho}=\rho/d_0$, and $\tilde{d}_0=d_0/W_0$.

The WKB predictions for the sidebranch amplitude and wavelength variations are obtained by substituting the mean shape $x_0(z)$, as well as the tip radius ρ and selection parameter σ^*, measured from the phase-field simulation results into Eqs. (21)–(23). Here, we use the actual tip radius, instead of the parabolic tip radius in the above equations. Since the tip radius cancels out in the exponent of Eq. (21), and it also cancels out in Eq. (22), this is of no consequence other than for the prefactor of Eq. (21) [see Eq. (23)]. It can be argued that the use of the actual tip radius in the prefactor is physically more meaningful, since Eq. (21) calculates the amplification of the noise originating at the very dendrite tip. More importantly, it should be emphasized that the prefactor of Eq. (21), $\overline{S}$, is only known up to some dimensionless

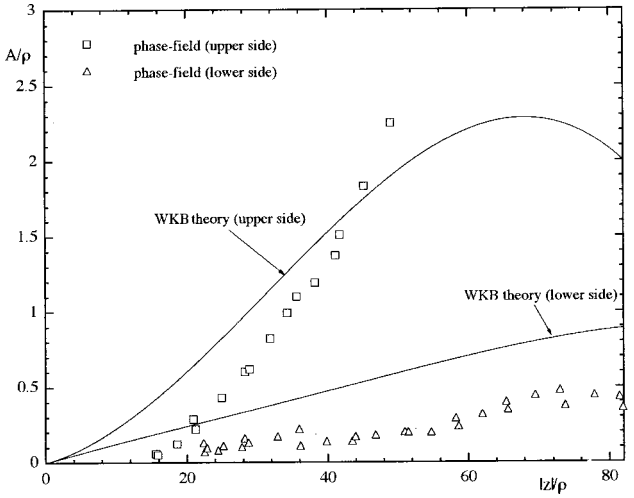

FIG. 15. Calculated sidebranch amplitudes for the upper and lower sides of the 45° growing dendrite arm ($Ud_0/D=0.135$, $F_u=1.25\times10^{-4}$, Pr=23.1, $\Delta=0.55$, and $\varepsilon=0.03$) as a function of distance behind the tip. The corresponding WKB predictions are plotted as different lines.

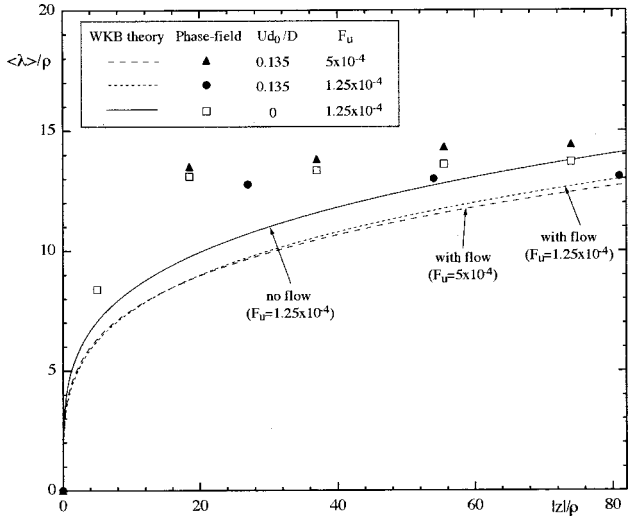

FIG. 16. Calculated mean sidebranch wavelengths for the upstream growing dendrite arm as a function of distance behind the tip for different flow velocities ($Ud_0/D=0$ and 0.135), different noise strengths ($F_u=1.25\times10^{-4}$ and 5×10^{-4}), and Pr=23.1, $\Delta=0.55$, and $\varepsilon=0.03$. The corresponding WKB predictions are plotted as different lines.

multiplicative constant of order unity [27]. For a weak anisotropy, and thus small σ^*, the sidebranching amplitude is dominated by the exponential amplification factor on the right-hand side of Eq. (21), and thus the distance behind the tip at which sidebranches first become visible [say, where $A(z)/\rho\sim0.1$ [27]] does not depend sensitively on the precise value of $\overline{S}$. Here, however, the anisotropy is relatively large and σ^* is itself of order unity. Thus, this distance depends more sensitively on the precise value of $\overline{S}$. Consequently, what is more relevant in the comparison shown next is the relative magnitudes of the sidebranching amplitudes in simulation and theory, rather than their exact agreement. Simulations for weaker anisotropies of 1% or less would be more appropriate for a precise quantitative comparison with WKB predictions but are comparatively much more costly. They remain an interesting prospect for the future.

Figure 14 shows a comparison of the phase-field results (symbols) with the WKB predictions (lines) for the variation of the scaled sidebranch amplitude as a function of dimensionless distance behind the tip for two noise strengths (1.25×10^{-4} and 5×10^{-4}). In addition to the phase-field results with flow from Figs. 8(c) and 9(c), data are included for a simulation without flow and the lower noise strength. As expected, the sidebranch amplitudes increase with increasing distance from the tip, and the higher noise strength results in larger amplitudes. For a given noise strength, the scaled amplitudes with flow are larger than without flow (the WKB prediction without flow for the higher noise strength can be obtained from Fig. 14 by simply multiplying the no-flow amplitudes shown for the lower noise strength by a factor of 2). Even though the form of the WKB relation for the amplitude variation, Eq. (21), remains unchanged in the presence of flow, flow affects the predicted scaled sidebranch amplitudes because it changes the tip-operating parameters (V, ρ, and σ^*) used in that equation. These changes in the tip-operating parameters explain the scaled amplitudes that are larger with flow than without. If instead of the actual tip radius, the parabolic tip radius and selection parameter were used in Eq. (21), flow would still affect the predicted amplitudes through the explicit appearance of the tip radius in the dimensionless noise amplitude $\overline{S}$ (note that, while the parabolic selection parameter is the same with and without flow, as shown in the preceding section, the parabolic tip radius changes with flow). Overall, the scaled amplitudes obtained from the various phase-field simulations with and without flow are in qualitative agreement with the corresponding predictions from the WKB theory. A more quantitative comparison is not possible due to the above-mentioned uncertainty in $\overline{S}$. In fact, the excellent agreement for the no-flow case in Fig. 14 may be coincidental.

We have also applied the WKB theory to explain the asymmetrical sidebranch amplitudes on the upstream (upper) and downstream (lower) sides of a dendrite arm growing at an angle with respect to the flow. The measured sidebranch amplitudes on both sides of the 45° growing dendrite arm shown in Fig. 13 are plotted in Fig. 15 together with the corresponding WKB predictions. The WKB predictions support the observation from the phase-field simulation that the amplitudes are larger on the upper side than on the lower side. Since the same dendrite tip parameters (V, ρ, and σ^*) are used in Eq. (21) for both sides, the difference in the amplitudes must be due to the different mean interface shapes of the upper and lower sides of the 45° growing dendrite. Since the upper side of the arm is wider than the lower side (where the width $\overline{x_0}$ is the distance between the growth axis and the noiseless interface in Fig. 13), Eq. (21) predicts larger amplitudes on the upper side than on the lower side. Even though the asymmetry in the mean shape between the upper and lower sides is relatively small, the fact that $A(z)\sim\exp(\overline{x_0}^{3/2})$ for a parabola results in large differences in the

amplitudes. This sensitivity of the sidebranch amplitudes to the mean shape has been emphasized by Brener and Temkin [28]. It should be noted that Eq. (21) is strictly not valid for the dendrite arm growing at an angle with respect to the flow. Since the flow is no longer in an axial direction, its effect on the advection of the perturbations along the crystal may no longer be negligibly small. Solvability and WKB sidebranching theories for the case in which the dendrite growth axis and the flow are not aligned are presently not available.

Numerical and theoretical results for the variation of the sidebranch wavelength with distance behind the tip are compared in Fig. 16. As expected from WKB theory, Eq. (22), the scaled wavelengths increase with distance behind the tip and are independent of the noise strength (to within the accuracy of the computed results). The scaled wavelengths measured from the phase-field simulations (symbols) are virtually the same with and without flow, which is qualitatively apparent also from Fig. 11. This relative independence of the scaled wavelengths on the flow strength is supported by the corresponding WKB predictions shown in Fig. 16 (lines). The WKB predictions with flow are only slightly below the one without flow, the difference being primarily due to the fact that σ^* is somewhat smaller with flow than without. It would be of interest also to compare the wavelengths for larger values of the flow parameter χ, where the ratio of selection parameters without to with flow becomes larger (Fig. 6). Figure 16 also shows that the phase-field results agree only roughly with the WKB theory for the wavelength variation, Eq. (22), and a relatively large disagreement exists close to the dendrite tip, even without flow. Karma and Rappel [43] have found that, in this case, the agreement between theory and numerical results could be improved in that region by incorporating the additional effect of the stretching of the wavelength of perturbations as they migrate from the tip to the sides. We suspect that the same effect is responsible here for the disagreement between simulations and the WKB theory, with flow.

VI. CONCLUSIONS

The effects of melt flow on the growth velocity, shape, and sidebranching dynamics of single dendritic crystals growing into a supercooled melt are quantitatively investigated in two dimensions using the phase-field method. The numerical results show that the flow causes the dendritic crystal to assume a highly asymmetric shape, which can be attributed to the strong effect of the direction of the flow relative to the growth axes. The flow increases the growth velocity of the arm growing upstream into the flow, has only a small effect on the arm growing normal to the flow, and retards the growth of the arm growing into the downstream direction in the wake of the crystal.

The phase-field results for the upstream growing dendrite reveal that an axial flow significantly changes the operating state of the dendrite tip. The ratio of the tip-selection parameters without and with flow, based on the actual tip radius, varies by about a factor of up to 2 over the range of flow velocities investigated. This result shows that the flow distorts the interface shape very near the tip and thus influences the actual tip radius ρ. Further away from the tip, however, flow leaves the interface shape parabolic and only influences the value of the tip radius ρ_p, obtained by fitting a parabola to this shape. This parabolic tip radius ρ_p, which corresponds to the tip radius typically measured experimentally in three dimensions, is in good agreement with the analytical two-dimensional Oseen-Ivantsov solution for the tip Peclet number and the linearized solvability theory of Bouissou and Pelce for the ratio of the selection parameters. The applicability of these theories, which assume a purely parabolic tip, may seem surprising. We note, however, that this nontrivial feature of the linearized theory is already present without flow. In this case, the theory predicts reasonably well the tip velocity over a comparable range of anisotropy in both two [49] and even three dimensions [50] *despite* the presence of a tip distortion already induced by anisotropic surface tension alone. We therefore conclude that the shape deviation from a parabola on a short distance scale from the tip of a fraction of ρ, which is controlled by both anisotropy and flow, does not significantly influence the tip velocity and the two-dimensional parabolic tip shape on a larger scale of ten tip radii.

Convection is also found to enhance the growth of the sidebranches along the upstream growing dendrite arm. The sidebranch amplitudes, scaled with the tip radius, obtained from the phase-field simulations are in qualitative agreement with predictions from WKB noise amplification theory. Even though flow does not change the WKB relation for the variation of the scaled sidebranch amplitude, the predicted scaled (and unscaled) amplitudes differ with and without flow because the tip-operating parameters used in the relation change due to flow. A completely quantitative comparison between the scaled sidebranch amplitudes from simulation and theory is prevented by the uncertainty in the prefactor of the WKB relation. Phase-field simulations of a dendrite growing at an angle with respect to the flow show that the sidebranch amplitudes grow much faster on the upstream side than on the downstream side. The comparison with WKB theory shows that this asymmetric behavior can be explained by the differences in the mean shape of the upstream and downstream sides of the inclined dendrite arm. Finally, the scaled sidebranch wavelengths obtained from phase-field simulations with and without flow show a similar variation with distance from the tip, indicating that the flow has little effect on the selection of the scaled critical wavelength. Any difference is again due to changes in the dendrite tip-operating parameters due to flow, whereas the WKB relation for the wavelength variation remains the same with and without flow. The scaled sidebranch wavelengths measured from the phase-field simulations show some disagreement with WKB theory near the dendrite tip both with and without flow. As in [43], we conclude that this is most likely due to the fact that the stretching of the wavelength of perturbations close to the tip has so far been neglected in WKB calculations of noise amplification [27,28,43].

The extension of the present work to three dimensions, weaker anisotropies, higher flow velocities, and lower supercoolings remains an important challenge for the future.

ACKNOWLEDGMENTS

We thank Professor Milovan Peric at the Universitat Hamburg, Germany, for generously providing us with the multigrid SIMPLE code that constituted the starting point of the present phase-field code with flow. We also thank Dr. Richard Hardin for his help with our computing facilities. This work was supported by the National Science Foundation (NSF) under Grant No. CTS-9501389 and NASA under Contract No. NCC8-94. The research of A.K. was also supported by U.S. DOE Grant No. DE-FG02-92ER45471.

[1] J. S. Langer, in *Chance and Matter*, edited by J. Souletie, J. Vannenimus, and R. Stora (North-Holland, Amsterdam, 1987), p. 629.
[2] D. Kessler, J. Koplik, and H. Levine, Adv. Phys. **37**, 255 (1988).
[3] E. A. Brener and V. I. Mel'nikov, Adv. Phys. **40**, 53 (1991).
[4] A. Karma and W.-J. Rappel, Phys. Rev. E **53**, R3017 (1996); **57**, 4323 (1998).
[5] N. Provatas, N. Goldenfeld, and J. Dantzig, Phys. Rev. Lett. **80**, 3308 (1998).
[6] A. Karma and W.-J. Rappel, Phys. Rev. Lett. **77**, 4050 (1996).
[7] S.-C. Huang and M. E. Glicksman, Acta Metall. **29**, 701 (1981); **29**, 717 (1981).
[8] M. E. Glicksman and S.-C. Huang, in *Convective Transport and Instability Phenomena*, edited by J. Zierip and H. Oertel, Jr. (G. Braun, Karlsruhe, West Germany, 1982), p. 557.
[9] M. E. Glicksman, S. R. Coriell, and G. B. McFadden, Annu. Rev. Fluid Mech. **18**, 307 (1986).
[10] Y. W. Lee, R. N. Smith, M. E. Glicksman, and M. B. Koss, Annu. Rev. Heat Transfer **VII**, 59 (1996).
[11] Ph. Bouissou, B. Perrin, and P. Tabeling, Phys. Rev. A **40**, 509 (1989).
[12] V. Emsellem and P. Tabeling, J. Cryst. Growth **156**, 285 (1995).
[13] Y. W. Lee, R. Ananth, and W. N. Gill, J. Cryst. Growth **132**, 226 (1993).
[14] R. Ananth and W. N. Gill, J. Cryst. Growth **179**, 263 (1997).
[15] B. Cantor and A. Vogel, J. Cryst. Growth **41**, 109 (1977).
[16] D. A. Saville and P. J. Beaghton, Phys. Rev. A **37**, 3423 (1988).
[17] M. Ben Amar, Ph. Bouissou, and P. Pelce, J. Cryst. Growth **92**, 97 (1988).
[18] R. Ananth and W. N. Gill, J. Cryst. Growth **91**, 587 (1988).
[19] R. Ananth and W. N. Gill, J. Cryst. Growth **108**, 173 (1991).
[20] J.-J. Xu, J. Fluid Mech. **263**, 227 (1994).
[21] R. J. Sekerka, S. R. Coriell, and G. B. McFadden, J. Cryst. Growth **154**, 370 (1995).
[22] M. Ben Amar and Y. Pomeau, PCH, PhysicoChem. Hydrodyn. **11**, 617 (1989).
[23] Ph. Bouissou and P. Pelce, Phys. Rev. A **40**, 6673 (1989).
[24] W. W. Mullins and R. F. Sekerka, J. Appl. Phys. **35**, 444 (1964).
[25] R. Pieters and J. S. Langer, Phys. Rev. Lett. **56**, 1948 (1986).
[26] M. N. Barber, A. Barbieri, and J. S. Langer, Phys. Rev. A **36**, 3340 (1987).
[27] J. S. Langer, Phys. Rev. A **36**, 3350 (1987).
[28] E. Brener and D. Temkin, Phys. Rev. E **51**, 351 (1995).
[29] A. Dougherty, P. D. Kaplan, and J. D. Gollub, Phys. Rev. Lett. **58**, 1652 (1987).
[30] Ph. Bouissou, A. Chiffaudel, B. Perrin, and P. Tabeling, Europhys. Lett. **13**, 89 (1990).
[31] U. Bisang and J. H. Bilgram, Phys. Rev. Lett. **21**, 3898 (1995).
[32] J. S. Langer, in *Directions in Condensed Matter*, edited by G. Grinstein and G. Mazenko (World Scientific, Singapore, 1986), p. 164.
[33] G. Caginalp, Phys. Rev. A **39**, 5887 (1989).
[34] G. B. McFadden, A. A. Wheeler, R. J. Braun, and S. R. Coriell, Phys. Rev. E **48**, 2016 (1993).
[35] R. Kobayashi, Physica D **63**, 410 (1993).
[36] A. A. Wheeler, B. T. Murray, and R. J. Schaefer, Physica D **66**, 243 (1993).
[37] J. A. Warren and W. J. Boettinger, Acta Metall. Mater. **43**, 689 (1995).
[38] S.-L. Wang and R. F. Sekerka, Phys. Rev. E **53**, 3760 (1996).
[39] C. Beckermann, H.-J. Diepers, I. Steinbach, A. Karma, and X. Tong, J. Comput. Phys. **154**, 468 (1999).
[40] R. Tönhardt and G. Amberg, J. Cryst. Growth **194**, 406 (1998); **213**, 161 (2000); Phys. Rev. E **62**, 828 (2000).
[41] D. M. Anderson, G. B. McFadden, and A. A. Wheeler, Physica D **135**, 175 (2000).
[42] X. Tong, C. Beckermann, and A. Karma, Phys. Rev. E **61**, R49 (2000).
[43] A. Karma and W. J. Rappel, Phys. Rev. E **60**, 3614 (1999).
[44] S. G. Pavlik and R. F. Sekerka, Physica A **268**, 283 (1999).
[45] A. Karma, Phys. Rev. Lett. **70**, 3439 (1993); Phys. Rev. E **48**, 3441 (1993).
[46] Z. Lilek, S. Muzaferija, and M. Peric, Numer. Heat Transfer, Part B **31**, 23 (1997).
[47] J. H. Ferziger and M. Peric, *Computational Methods in Fluid Mechanics* (Springer, Berlin, 1997).
[48] S. V. Patankar, *Numerical Heat Transfer and Fluid Flow* (Hemisphere, Washington, D.C., 1980).
[49] A. Barbieri and J. S. Langer, Phys. Rev. A **39**, 5314 (1989).
[50] A. Karma, Y. H. Lee, and M. Plapp, Phys. Rev. E **61**, 3996 (2000).